

Uncertainty and Reliability Analysis of Fluid–Structure Stability Boundaries

Clemens V. Verhoosel,* Thomas P. Scholcz,† Steven J. Hulshoff,‡ and Miguel A. Gutiérrez§
Delft University of Technology, 2600 GB Delft, The Netherlands

DOI: 10.2514/1.35770

Fluid–structure interactions provide design constraints in many fields, yet methods available for their analysis normally assume that the structural properties are exactly known. In this contribution, these properties are more realistically modeled using random fields. Stochastic finite element methods are applied to perform uncertainty and reliability analysis on fluid–structure interaction problems with random input parameters. As an example we consider panel divergence and panel flutter. Numerical simulations demonstrate the appropriateness of sensitivity-based methods for characterization of the statistical moments of the critical points as well as for the determination of the probability of occurrence of undesired phenomena.

Nomenclature

\mathbf{a}	= discrete solution vector
a_∞	= freestream fluid speed of sound
\mathbf{C}	= damping matrix of the coupled system
C_y	= confidence level of sampled variable \tilde{y}
C_y^*	= confidence level of \tilde{y} with discretization error
E	= modulus of elasticity
\mathbf{f}	= right-hand side vector
h	= panel length
\mathbf{K}	= stiffness matrix of the coupled system
l_c	= characteristic length of the random field
\mathbf{M}	= mass matrix of the coupled system
m	= number of random variables used for random field parametrization
M_{cr}	= critical Mach number
M_{div}	= divergence Mach number
M_{fl}	= flutter Mach number
M_{lim}	= prescribed critical Mach number
M_∞	= freestream fluid Mach number
n	= number of degrees of freedom
n_y^s	= sample size used for the sampling of \tilde{y}
N_x, N_y	= number of finite difference points in the horizontal and the vertical direction
\mathcal{P}_{fail}	= probability of failure
p_∞	= freestream fluid pressure
t_p	= panel thickness
u_∞	= freestream horizontal fluid velocity
u	= horizontal velocity of the fluid
v	= vertical velocity of the velocity
V_y	= coefficient of variation of random variable \tilde{y}
w	= vertical displacement of the panel
$\mathbf{x}_{i,j}$	= position of finite difference point (i, j)
$\tilde{\mathbf{z}}$	= vector of standard Gaussian random variables
Δx	= finite difference grid spacing
δ_i, ω_i	= real and imaginary part of the coupled system eigenvalue λ_i
ξ	= vector of physical parameters

$\zeta_i, \hat{r}_i(x)$	= i th eigenvalue and corresponding eigenfunction of the covariance function
$\lambda_i, \hat{\mathbf{a}}_i$	= i th eigenvalue and corresponding eigenvector of coupled system
μ_y	= mean of random variable \tilde{y}
ν	= Poisson ratio
ρ_p	= density of the panel
ρ_∞	= freestream fluid density
$\varrho_Y(x_1, x_2)$	= spatial correlation function of random field $\tilde{Y}(x)$
σ_y	= standard deviation of random variable \tilde{y}
$\Phi(\mathbf{z})$	= cumulative density function of standard Gaussian random vector $\tilde{\mathbf{z}}$
ϕ	= perturbation of fluid potential
$\varphi(\mathbf{z})$	= probability density function of standard Gaussian random vector $\tilde{\mathbf{z}}$

Subscript

p	= quantity related to the panel
-----	---------------------------------

Superscript

f	= quantity related to the fluid
p	= quantity related to the panel
$*$	= quantity related to the design point

Special Symbols

\sim	= random quantity
$-$	= statistical quantity obtained by sampling

I. Introduction

FLUID–structure interactions play an important role in many fields. Because unstable interactions can cause structural failure, prediction of their occurrence is of primary importance in the design of aircraft and many other structures.

Fluid–structure interactions have been studied extensively, which has resulted in several analytical and numerical methods for their prediction [1–3]. Generally, these methods presume that the properties of the structure are exactly known. In reality, structural properties are not known exactly due to the presence of microscopic material imperfections, variations in manufacturing, material degradation due to corrosion, and many other sources of uncertainty. In practice, these uncertainties are taken into account indirectly by using conservative safety factors. Direct incorporation of uncertainties in the analysis of fluid–structure interactions should therefore result in more efficient designs.

In this contribution the analysis of fluid–structure interactions with structural uncertainties is performed using stochastic finite element

Received 20 November 2007; revision received 5 September 2008; accepted for publication 5 September 2008. Copyright © 2008 by the American Institute of Aeronautics and Astronautics, Inc. All rights reserved. Copies of this paper may be made for personal or internal use, on condition that the copier pay the \$10.00 per-copy fee to the Copyright Clearance Center, Inc., 222 Rosewood Drive, Danvers, MA 01923; include the code 0001-1452/09 \$10.00 in correspondence with the CCC.

*Ph.D. Candidate, Faculty of Aerospace Engineering.

†M.S. Student, Faculty of Aerospace Engineering.

‡Assistant Professor, Faculty of Aerospace Engineering.

§Professor, Faculty of Mechanical, Maritime and Materials Engineering; m.a.gutierrez@tudelft.nl.

methods (SFEM) [4]. These methods can be regarded as extensions of the deterministic finite element method, which makes them suitable for implementation in existing software packages. Divergence and flutter of a panel [5,6] with a random field of elastic properties is considered as a test case. The Mach numbers at which divergence or flutter occurs are referred to as the divergence and flutter critical points. We describe methods for determining the statistical moments of these critical points, as well as the probability of the occurrence of undesired behavior below a specified Mach number.

In the following section, the basic discretization of the deterministic panel problem and computation of the critical points is discussed. The considered stochastic methods are then introduced in Sec. III. The computation of sensitivities of the instability boundaries, as required by some of the stochastic finite element models, is discussed in Sec. IV. Numerical simulations are performed in Sec. V to demonstrate the applicability of SFEM to the fluid–structure interaction problem. Finally, some conclusions are drawn in Sec. VI.

II. Deterministic Fluid–Structure Interaction Model

A monolithically coupled fluid–structure model is developed for the analysis of the panel problem. The equations of motion of the structure and the fluid are discretized using the finite element method and finite difference method, respectively. This approach allows for extension of the model by considering complex geometries or more sophisticated fluid and structure descriptions.

The basic configuration of the panel problem is shown in Fig. 1. A plate is clamped between two rigid surfaces. A fluid is flowing over the plate and is considered in a domain of size $5 \times 3h$. The pressure under the plate is assumed to be undisturbed with respect to the freestream conditions. For notational convenience, the physical properties of both structure and fluid are assembled in a vector of properties

$$\xi = [p_\infty, \rho_\infty, a_\infty, t_p, \rho_p, E, \nu]^T \quad (1)$$

It should be noted that (again for notational convenience) the freestream Mach number is not included in this vector.

The deterministic discretization of the panel and the fluid is considered in Sec. II.A and II.B. The fluid–structure coupling is described in Sec. II.C, and a coupled system of equations is formulated in Sec. II.D. Mathematical definitions of the critical points are obtained and validated in Sec. II.E.

A. Discrete Representation of the Motion of the Plate

The motion of the plate shown in Fig. 1 is governed by the Euler–Bernoulli beam equation

$$\rho_p t_p \frac{\partial^2 w}{\partial t^2} + \frac{\partial^2}{\partial x^2} \left[\frac{EI}{1 - \nu^2} \frac{\partial^2 w}{\partial x^2} \right] = -\Delta p(x) \quad (2)$$

where $I = \frac{1}{12} t_p^3$ is the cross-sectional moment of inertia per unit length of the panel and $\Delta p(x) = p(x) - p_\infty$ is the pressure difference over the panel. This equation is discretized by derivation of its weak form, which is obtained by multiplication with a

kinematically admissible test function γ and integrated over the length of the plate to yield

$$\int_{-h/2}^{h/2} \left(\rho_p t_p \frac{\partial^2 w}{\partial t^2} + \frac{\partial^2}{\partial x^2} \left[\frac{EI}{1 - \nu^2} \frac{\partial^2 w}{\partial x^2} \right] \right) \gamma dx = - \int_{-h/2}^{h/2} \Delta p(x) \gamma dx \quad (3)$$

Integrating by parts twice then gives

$$\begin{aligned} \int_{-h/2}^{h/2} \rho_p t_p \frac{\partial^2 w}{\partial t^2} \gamma dx + \int_{-h/2}^{h/2} \frac{EI}{1 - \nu^2} \frac{\partial^2 w}{\partial x^2} \frac{\partial^2 \gamma}{\partial x^2} dx \\ = - \int_{-h/2}^{h/2} \Delta p(x) \gamma dx \end{aligned} \quad (4)$$

where use is made of the boundary conditions $w(-h/2) = w(h/2) = 0$ and $dw/dx(-h/2) = dw/dx(h/2) = 0$. Because second-order derivatives are present in this equation, Hermitian shape functions $\psi(x)$ are used to discretize the displacement field as

$$w(x) \approx \sum_{i=1}^{n_p} \psi_i(x) a_i^p \quad (5)$$

where \mathbf{a}^p contains both the nodal displacements and nodal rotations. Substitution of this expression in the weak form in Eq. (4) and using the Hermitian shape functions as test functions yields a set of n_p discrete equations

$$\mathbf{M}^{pp} \ddot{\mathbf{a}}^p + \mathbf{K}^{pp} \mathbf{a}^p = \mathbf{f}^p \quad (6)$$

where

$$M_{ij}^{pp}(\xi) = \int_{-h/2}^{h/2} \rho_p t_p \psi_i \psi_j dx \quad (7)$$

$$K_{ij}^{pp}(\xi) = \int_{-h/2}^{h/2} \frac{EI}{1 - \nu^2} \frac{\partial^2 \psi_i}{\partial x^2} \frac{\partial^2 \psi_j}{\partial x^2} dx \quad (8)$$

$$f_i^p(\xi) = - \int_{-h/2}^{h/2} \Delta p(x) \psi_i dx \quad (9)$$

for $i, j = 1, \dots, n_p$.

B. Discretization of the Fluid Motion

The fluid is assumed to be governed by the two-dimensional unsteady linearized potential equation

$$(1 - M_\infty^2) \frac{\partial^2 \phi}{\partial x^2} + \frac{\partial^2 \phi}{\partial y^2} - \frac{1}{a_\infty^2} \left(\frac{\partial^2 \phi}{\partial t^2} + 2u_\infty \frac{\partial^2 \phi}{\partial x \partial t} \right) = 0 \quad (10)$$

where the horizontal and vertical velocity fields are given by

$$u = u_\infty + \frac{\partial \phi}{\partial x} \quad \text{and} \quad v = \frac{\partial \phi}{\partial y} \quad (11)$$

respectively. The linearized potential Eq. (10) is valid for subsonic flow and supersonic flow but is not applicable in the transonic regime [7].

Because the type of the linearized potential equation changes from elliptic for subsonic Mach numbers to hyperbolic for supersonic Mach numbers, two different sets of far field boundary conditions need to be defined. In the subsonic case, the far field perturbation is assumed to be zero ($\phi = 0$). In the supersonic case, both the perturbation potential and horizontal perturbation velocity are zero on the inflow boundary ($\phi = \partial \phi / \partial x = 0$) and the perturbation potential is zero ($\phi = 0$) on the upper boundary. The latter boundary condition is only valid if the Mach line from the panel leading edge does not intersect the upper boundary, which requires the Mach angle with respect to the freestream flow direction to be smaller than 45 deg

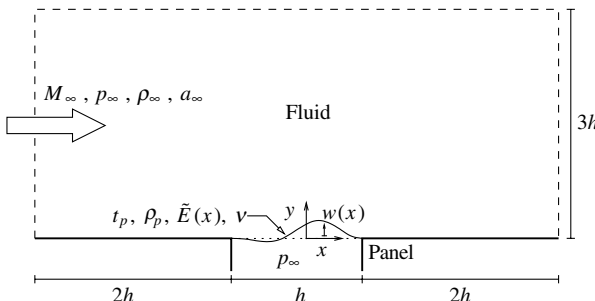


Fig. 1 Schematic representation of the panel problem.

for the fluid domain considered here (i.e., the freestream Mach number M_∞ should be larger than approximately 1.4).

The partial differential Eq. (10) is discretized using the finite difference method. Because of variations in the behavior of the differential equation, different finite difference schemes need to be implemented. In the subsonic case, a second-order central scheme is used for both directions (Table 1). In the supersonic case, a first-order upwind scheme is used in the horizontal direction and a second-order central scheme in the vertical direction (Table 1).

The discrete equation of motion of the fluid is obtained by assembling the finite difference equations for all points in the finite difference grid, as shown in Fig. 2, to yield a system of the form

$$\mathbf{M}^{ff}\ddot{\mathbf{a}}^f + \mathbf{C}^{ff}\dot{\mathbf{a}}^f + \mathbf{K}^{ff}\mathbf{a}^f = \mathbf{f}^f \quad (12)$$

C. Fluid–Structure Coupling

The pressure difference between the upper and lower side of the panel is given by

$$\Delta p(x) = -\rho_\infty \left(\frac{\partial \phi}{\partial t} + u_\infty \frac{\partial \phi}{\partial x} \right) \quad (13)$$

This pressure difference can be expressed in terms of the discrete fluid-potential vector \mathbf{a}_f and its temporal derivative as

$$\Delta p(x) = \mathbf{g}^f(x)^T \dot{\mathbf{a}}^f + \mathbf{h}^f(x)^T \mathbf{a}^f \quad (14)$$

where the vectors $\mathbf{g}_f(x)$ and $\mathbf{h}_f(x)$ can be regarded as shape functions that map the discrete potential onto the continuous pressure difference across the plate.

The fluid is influenced by the panel via the boundary conditions. As can be seen in Table 1, the finite difference equations for the nodes on the bottom are influenced by the vertical velocity of the bottom $v(\mathbf{x}_{i,1})$. For $x \leq -h/2$ or $x \geq h/2$ this velocity is zero because the solid base does not move in vertical direction. For $-h/2 < x < h/2$, the flow should be tangent to the panel, which is moving upward with velocity $\dot{w}(x)$. In other words, a fluid particle flowing over the plate should have the same vertical velocity as the plate. This results in

$$v(\mathbf{x}_{i,1}) = \frac{\partial w}{\partial t} + u_\infty \frac{\partial w}{\partial x} \quad (15)$$

where Eq. (11) is used with the assumption that the horizontal perturbation is to be negligible compared with the freestream condition ($\partial \phi / \partial x \ll u_\infty$). The vertical velocity of the fluid over the plate can then be expressed in terms of the discrete nodal displacements and displacement rates of the plate as

$$v(\mathbf{x}_{i,1}) = \mathbf{g}^p(\mathbf{x}_{i,1})^T \dot{\mathbf{a}}^p + \mathbf{h}^p(\mathbf{x}_{i,1})^T \mathbf{a}^p \quad (16)$$

where the vectors \mathbf{g}^p and \mathbf{h}^p can be seen as shape functions that map the discrete displacements and rotations of the plate onto the continuous vertical velocity of the fluid.

D. Monolithically Coupled Fluid–Structure Model

For the results computed here, the fluid and structure are coupled monolithically (i.e., the equations describing the motion of both the fluid and structure are combined into a single system of equations that are solved simultaneously). The monolithic system is obtained by substitution of the discretized pressure difference Eq. (14) into the expression for the external force of the plate Eq. (9) to yield

$$\begin{aligned} \mathbf{f}^p = & - \int_{-h/2}^{h/2} \psi(x) \mathbf{g}^f(x)^T dx \dot{\mathbf{a}}^f \\ & - \int_{-h/2}^{h/2} \psi(x) \mathbf{h}^f(x)^T dx \mathbf{a}^f \quad \text{for } i = 1, \dots, n_p \end{aligned} \quad (17)$$

which implies that the external force on the plate can be written as

$$\mathbf{f}^p = -\mathbf{C}^{pf}\dot{\mathbf{a}}^f - \mathbf{K}^{pf}\mathbf{a}^f \quad (18)$$

Similarly, the expression for the boundary velocity Eq. (16) is used to complete the finite difference scheme for the fluid. The boundary condition vector can be expressed as

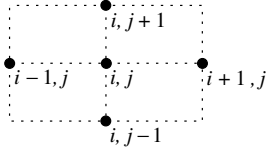
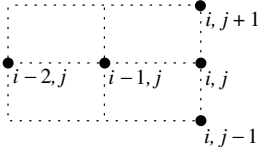
$$\mathbf{f}^f = -\mathbf{C}^{fp}\dot{\mathbf{a}}^p - \mathbf{K}^{fp}\mathbf{a}^p \quad (19)$$

Combining the equations of motion of the plate in Eq. (6) and fluid in Eq. (12) with the expressions in Eqs. (18) and (19) then yields the coupled equation of motion

$$\mathbf{M}(\xi)\ddot{\mathbf{a}} + \mathbf{C}(M_\infty, \xi)\dot{\mathbf{a}} + \mathbf{K}(M_\infty, \xi)\mathbf{a} = \mathbf{0} \quad (20)$$

with $\mathbf{a} = [\mathbf{a}^p \quad \mathbf{a}^f]^T$ and

Table 1 Finite difference schemes as used for the discretization of the linearized potential equation. The grid spacing Δx and Δy are used as defined in Fig. 2.

	Subsonic	Supersonic
		
$\phi(\mathbf{x}_{i,j})$	$\phi_{i,j}$	$\phi_{i,j}$
$\frac{\partial \phi}{\partial x}(\mathbf{x}_{i,j})$	$\frac{\phi_{i+1,j} - \phi_{i-1,j}}{2\Delta x}$	$\frac{\phi_{i,j} - \phi_{i-1,j}}{\Delta x}$
$\frac{\partial \phi}{\partial x}(\mathbf{x}_{1,j})$	$\frac{\phi_{2,j}}{2\Delta x}$	$\frac{\phi_{1,j}}{\Delta x}$
$\frac{\partial \phi}{\partial x}(\mathbf{x}_{N_x,j})$	$-\frac{\phi_{N_x,j} - \phi_{N_x-1,j}}{2\Delta x}$	$\frac{\phi_{N_x,j} - \phi_{N_x-1,j}}{\Delta x}$
$\frac{\partial^2 \phi}{\partial x^2}(\mathbf{x}_{i,j})$	$\frac{\phi_{i-1,j} - 2\phi_{i,j} + \phi_{i+1,j}}{\Delta x^2}$	$\frac{\phi_{i-2,j} - 2\phi_{i-1,j} + \phi_{i,j}}{\Delta x^2}$
$\frac{\partial^2 \phi}{\partial x^2}(\mathbf{x}_{1,j})$	$-\frac{2\phi_{1,j} + \phi_{2,j}}{\Delta x^2}$	$\frac{\phi_{1,j}}{\Delta x^2}$
$\frac{\partial^2 \phi}{\partial x^2}(\mathbf{x}_{2,j})$	$\frac{\phi_{1,j} - 2\phi_{2,j} + \phi_{3,j}}{\Delta x^2}$	$-\frac{2\phi_{1,j} + \phi_{2,j}}{\Delta x^2}$
$\frac{\partial^2 \phi}{\partial x^2}(\mathbf{x}_{N_x,j})$	$\frac{\phi_{N_x-1,j} - 2\phi_{N_x,j} + \phi_{N_x+1,j}}{\Delta x^2}$	$\frac{\phi_{N_x-2,j} - 2\phi_{N_x-1,j} + \phi_{N_x,j}}{\Delta x^2}$
$\frac{\partial^2 \phi}{\partial y^2}(\mathbf{x}_{i,j})$	$\frac{\phi_{i,j-1} - 2\phi_{i,j} + \phi_{i,j+1}}{\Delta y^2}$	$\frac{\phi_{i,j-1} - 2\phi_{i,j} + \phi_{i,j+1}}{\Delta y^2}$
$\frac{\partial^2 \phi}{\partial y^2}(\mathbf{x}_{i,1})$	$\frac{2\phi_{i,2} - 2\phi_{i,1}}{\Delta y^2} - \frac{2v(\mathbf{x}_{i,1})}{\Delta y}$	$\frac{2\phi_{i,2} - 2\phi_{i,1}}{\Delta y^2} - \frac{2v(\mathbf{x}_{i,1})}{\Delta y}$
$\frac{\partial^2 \phi}{\partial y^2}(\mathbf{x}_{i,N_y})$	$\frac{\phi_{i,N_y-1} - 2\phi_{i,N_y}}{\Delta y^2}$	$\frac{\phi_{i,N_y-1} - 2\phi_{i,N_y}}{\Delta y^2}$

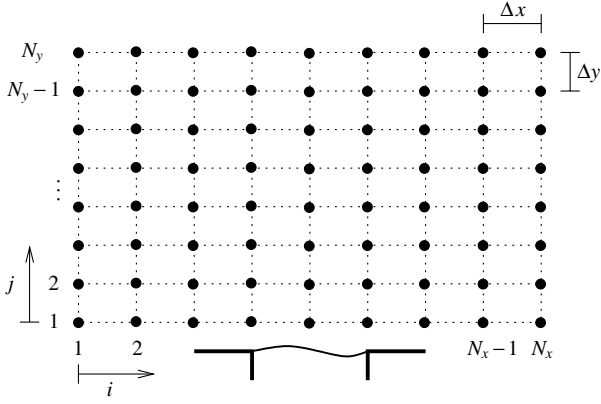


Fig. 2 Finite difference grid of $N_x \times N_y$ points used for the discretization of the fluid.

$$\begin{aligned} \mathbf{M} &= \begin{bmatrix} \mathbf{M}^{pp} & 0 \\ 0 & \mathbf{M}^{ff} \end{bmatrix} \\ \mathbf{C} &= \begin{bmatrix} 0 & \mathbf{C}^{pf} \\ \mathbf{C}^{fp} & \mathbf{C}^{ff} \end{bmatrix} \\ \mathbf{K} &= \begin{bmatrix} \mathbf{K}^{pp} & \mathbf{K}^{pf} \\ \mathbf{K}^{fp} & \mathbf{K}^{ff} \end{bmatrix} \end{aligned} \quad (21)$$

E. Stability Boundaries

Two types of fluid–structure instabilities are considered. The first is aeroelastic divergence, which for the panel problem typically occurs at subsonic speeds. The second is aeroelastic flutter, which typically occurs at supersonic speeds [8].

1. Divergence

Divergence is regarded as a static instability [1]. Therefore the rate-dependent terms in the equation of motion in Eq. (20) can be neglected, resulting in the linear system

$$\mathbf{K}(\mathbf{M}_\infty, \xi) \mathbf{a} = \mathbf{0} \quad (22)$$

Nontrivial solutions for \mathbf{a} only exist in the case that the stiffness matrix \mathbf{K} of the coupled fluid–structure model is singular (i.e., has a zero eigenvalue). Because the matrix \mathbf{K} depends on the Mach number and modulus of elasticity, the smallest (in magnitude) eigenvalue can be written as

$$|\lambda_1| = |\lambda_1|(\mathbf{M}_\infty, \xi) \quad (23)$$

where the eigenvalues of \mathbf{K} are sorted with ascending magnitude ($|\lambda_1| < |\lambda_2| < \dots < |\lambda_N|$). The divergence Mach number is defined as the smallest Mach number for which $|\lambda_1|$ is zero, which results in an implicit definition of the divergence Mach number as

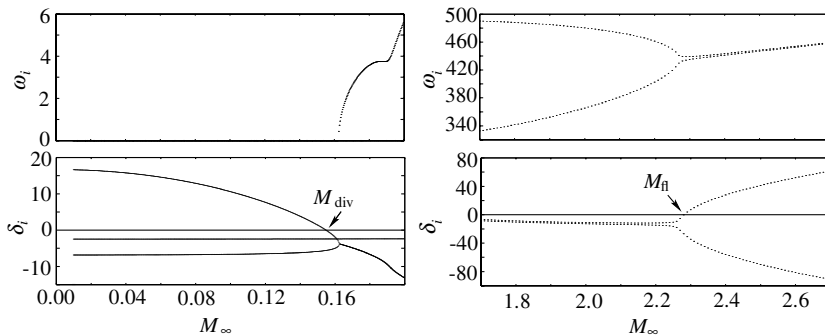


Fig. 3 Divergence diagram (left) and flutter diagram (right) corresponding to the parameters assembled in Table 2. The critical Mach numbers can be found by determining the point at which the real part of one of the eigenvalues is equal to zero.

$$|\lambda_1|(\mathbf{M}_{\text{div}}, \xi) = 0 \quad (24)$$

The divergence point can easily be determined by plotting the real and imaginary parts of the eigenvalues, $\delta_i = \text{Re}(\lambda_i)$ and $\omega_i = \text{Im}(\lambda_i)$, vs the Mach number (Fig. 3). From the diagram an approximate initial guess of the divergence point is obtained. The critical point is then determined with a specified tolerance using a Newton–Raphson procedure.

The deterministic computation of the divergence point is tested using a case with subsonic flow. The case parameters are given in Table 2. Analytical solutions for the divergence speed have been previously obtained by various authors. In Kornecki et al. [5], for example, it is proposed to compute the critical Mach number using

$$M_{\text{div}} = 177 \cdot \sqrt{\frac{1}{\rho_\infty a_\infty^2} \frac{E}{1 - \nu^2} \frac{I}{h^3}} \quad (25)$$

Evaluating this expression using the parameters in Table 2, the divergence Mach number is found to be $M_{\text{div}} \approx 0.1491$. The solution obtained on the 321×193 grid is equal $M_{\text{div}} \approx 0.149$, which compares favorably with the analytical result. The corresponding potential field and divergence mode of the panel are shown in Fig. 4. Computation of this divergence Mach number on this grid takes about 50 s on a 2.8 GHz Quad-Core Intel Xeon 5400 series processor.

A mesh convergence analysis is performed in order to obtain an error estimate of the numerical result. The relative error of the critical Mach number is defined as

$$\epsilon_{M_{\text{cr}}} = \frac{M_{\text{cr}}(\Delta) - M_{\text{cr}}(\Delta_{\text{res}})}{M_{\text{cr}}(\Delta_{\text{res}})} \quad (26)$$

with Δ_{res} being the grid spacing on a Cartesian grid ($\Delta x = \Delta y = \Delta$) with 641×385 grid points, which is assumed to be fully resolved. This error is depicted for various discretizations in Fig. 5. As can be seen, the relative error for the 321×193 mesh is equal to 6.6×10^{-4} and falls within the asymptotic region of convergence of the fluid–structure discretization.

Remark 1: It is important to note that for the determination of the divergence point, only the smallest in magnitude eigenvalue is required. Because large systems are considered in this contribution (up to approximately 1.5×10^5 degrees of freedom), the computation of all eigenvalues is computationally intractable. Instead, only the smallest eigenvalue is computed using standard algorithms (e.g., Matlab’s eigs).

2. Flutter

Flutter is regarded as a dynamic instability [1]. Its associated stability boundary can be found by substitution of the harmonic solution

$$\mathbf{a} = \sum_{i=1}^n \hat{\mathbf{a}}_i e^{\lambda_i t} \quad (27)$$

into the equation of motion in Eq. (20) to yield the quadratic eigenvalue problem

Table 2 Parameters used for the validation of the deterministic fluid–structure interaction model

	Divergence	Flutter	
h	0.5	0.5	m
t_p	0.675	1.35	mm
ρ_p	-	2710	kg/m ³
E	77.28	77.28	GPa
ν	0.33	0.33	
ρ_∞	1.225	0.4000	kg/m ³
a_∞	340	300	m/s

$$[\lambda_i^2 \mathbf{M}(\xi) + \lambda_i \mathbf{C}(M_\infty, \xi) + \mathbf{K}(M_\infty, \xi)] \hat{\mathbf{a}}_i = \mathbf{0} \quad \text{for } i = 1, \dots, n \quad (28)$$

The eigenvalues of this system are generally complex and are sorted with descending real part ($\delta_1 > \delta_2 > \dots > \delta_n$). Because the matrix \mathbf{K} depends on both the properties vector ξ and the freestream Mach number, the largest real part of an eigenvalue can be written as

$$\delta_1 = \delta_1(M_\infty, \xi) \quad (29)$$

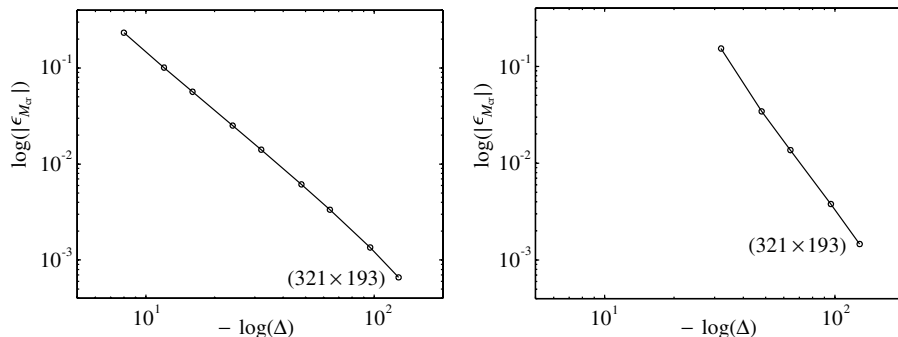
The harmonic solution in Eq. (27) is stable in the case that all real parts of the eigenvalues are negative. Hence, the critical Mach number at which flutter occurs is defined by the requirement that δ_1 equals zero, leading to the implicit flutter definition

$$\delta_1(M_\Pi, \xi) = 0 \quad (30)$$

This definition is very similar to the definition of the divergence speed in Eq. (24). The determination of the flutter point is therefore done in the same way as for the divergence point. The flutter diagram required to make an initial guess for the critical Mach number is shown in Fig. 3.

The flutter test case considered here is the same as considered in [6], and the parameters used are assembled in Table 2. The proposed method yields $M_\Pi \approx 2.27$ for a grid with 321×193 points, which matches the flutter point obtained in [6]. The corresponding mode of the panel and potential field are shown in Fig. 4. The computation of the flutter point for this grid takes approximately 150 s for the configuration mentioned previously.

A mesh convergence study is performed, and its results are presented in Fig. 5. The relative error as defined in Eq. (26) is shown

**Fig. 4** Disturbance potential and mode shape for subsonic divergence (left) and supersonic flutter (right) corresponding to the parameters in Table 2.**Fig. 5** Mesh convergence plots for the critical Mach number for divergence (left) and flutter (right) corresponding to the parameters in Table 2.

for various grids. The relative error on a 321×193 grid is equal to 1.5×10^{-3} and falls in the asymptotic region of convergence.

Remark 2: As in the case of divergence, only one (or a few) eigenvalues are required in order to determine the flutter point. The quadratic eigenvalue problem in Eq. (28) is solved by transforming it into a linear eigenvalue problem with twice the original problem size. Appropriate scaling of the transformed system [9] is used to obtain robust results.

III. Stochastic Finite Element Analysis

Existing studies of the panel problem assume the properties of the plate to be exactly known (i.e., the problem is considered to be deterministic). In reality, various sources of randomness are present. These uncertainties can have a significant influence on the stability boundaries and are therefore important to study.

Here, the modulus of elasticity of the plate is considered to be random. Material properties such as the Young's modulus can be described by a random field $\tilde{E}(x)$. Consequently, the vector of properties of the panel problem in Eq. (1) is represented by a random vector

$$\tilde{\xi} = [p_\infty, \rho_\infty, a_\infty, t_p, \rho_p, \tilde{E}(x), \nu]^T \quad (31)$$

From the definitions of the divergence point in Eq. (24) and flutter point in Eq. (30), it follows that the critical Mach numbers depend on the vector of model properties. Because this vector is random, the critical Mach numbers

$$\tilde{M}_{cr} = M_{cr}(\tilde{\xi}) \quad (32)$$

are also random.

SFEM are considered as finite element methods for solving problems with random input parameters, in this case the modulus of elasticity. The representation of this random field is considered in Sec. III.A. Stochastic finite element methods are used for determination of the statistical moments (mean, standard deviation, etc.) of the critical points as well as for the computation of the probability of occurrence of divergence or flutter below a specified Mach number. The former type of analysis is referred to as uncertainty analysis and is discussed in Sec. III.B. The latter type of stochastic analysis is known as reliability analysis and is treated in Sec. III.C.

A. Discrete Representation of the Random Field of Elastic Properties

The Young's modulus can be modeled appropriately using a stationary lognormal random field [10]. This allows the fact that the Young's modulus is strictly positive from a physical point of view to be correctly represented.

A parametrization of the random field of elastic properties $\tilde{E}(x)$ is required in order to analyze the problem. This parametrization is obtained by defining an underlying stationary Gaussian field

$$\tilde{G}(x) = \ln(\tilde{E}(x)) \quad (33)$$

with

$$\mu_G = \ln(\mu_E) - \frac{1}{2} \ln(1 + V_E^2) \quad \text{and} \quad \sigma_G^2 = \ln(1 + V_E^2) \quad (34)$$

The autocorrelation function of the underlying Gaussian field $\tilde{G}(x)$ can be exactly related to the properties of the lognormal field [11] by

$$\varrho_G(x_1, x_2) = \frac{\ln(1 + \varrho_E(x_1, x_2) V_E^2)}{\ln(1 + V_E^2)} \quad (35)$$

and is shown in Fig. 6. In the case that properties other than the modulus of elasticity need to be described by random fields, other distributions (e.g., Weibull) might be required. An exact expression for the correlation of the underlying Gaussian field cannot be obtained for most distributions other than lognormal. Approximate expressions are, however, available for many other distributions [11].

The parametrization of the Gaussian field $\tilde{G}(x)$ is obtained by the truncated Karhunen–Loeve expansion [12] as

$$\tilde{G}(x) \approx G(x, \tilde{\mathbf{z}}) = \mu_G + \sum_{i=1}^m \sqrt{\zeta_i} \hat{r}_i(x) \tilde{z}_i \quad (36)$$

with ζ_i and $\hat{r}_i(x)$ being the eigenvalues and eigenfunctions of the covariance function $\sigma_G^2 \varrho_G(x_1, x_2)$. Here the Karhunen–Loeve eigenvalues and eigenfunctions are determined numerically [13].

Because an m -dimensional parametrization of the Gaussian field $\tilde{G}(x)$ is obtained, a parametrization of the lognormal field $\tilde{E}(x)$ follows by application of the inverse of the transformation in Eq. (33) to yield

$$\tilde{E}(x) \approx E(x, \tilde{\mathbf{z}}) = \frac{\mu_E}{\sqrt{1 + V_E^2}} \prod_{i=1}^m \exp(\sqrt{\zeta_i} \hat{r}_i(x) \tilde{z}_i) \quad (37)$$

B. Uncertainty Analysis

The statistical moments of the critical Mach number are computed by two methods: the sampling-based crude Monte Carlo method and the sensitivity-based perturbation method. Uncertainty analysis for the panel flutter point using an analytical expression for the aerodynamic operator has been addressed in [14]. The methods considered here are based on a numerically discretized fluid domain, which makes them more generally applicable.

1. Crude Monte-Carlo Method

The statistical moments of the critical Mach number can be obtained using the crude Monte-Carlo method. In this method, realizations of the field of elastic properties in Eq. (37) are sampled, and the critical Mach number is determined for each realization. The mean critical Mach number and its standard deviation is obtained from the sample by

$$\begin{aligned} \bar{\mu}_{M_{cr}} &= \frac{1}{n_{\mu_{M_{cr}}}^s} \sum_{i=1}^{n_{\mu_{M_{cr}}}^s} M_{cr}(\mathbf{z}_i) \quad \text{and} \\ \bar{\sigma}_{M_{cr}} &= \sqrt{\frac{1}{n_{\sigma_{M_{cr}}}^s} \sum_{i=1}^{n_{\sigma_{M_{cr}}}^s} (M_{cr}(\mathbf{z}_i) - \bar{\mu}_{M_{cr}})^2} \end{aligned} \quad (38)$$

The accuracy of the estimates for the mean and standard deviation of the critical Mach number obviously depends on the sample sizes n^s . The required sample size depends on 1) the required accuracy of the statistical moments, and 2) the distribution of the response, in this case the critical Mach number.

The required accuracy is commonly specified by a confidence level C , defined for the mean of the critical Mach number as

$$\Pr \left[\left| \frac{\bar{\mu}_{M_{cr}} - \mu_{M_{cr}}}{\mu_{M_{cr}}} \right| \geq 1 - C_{\mu_{M_{cr}}} \right] \leq 1 - C_{\mu_{M_{cr}}} \quad (39)$$

A similar expression can be written for its standard deviation. An a priori estimate of the sample size required for the approximation of the mean with a confidence level C is given by [15]

$$n_{\mu_{M_{cr}}}^s \geq \left(\frac{\Phi^{-1} \left(\frac{1 + C_{\mu_{M_{cr}}}}{2} \right)}{1 - C_{\mu_{M_{cr}}}} \right)^2 V_{\bar{\mu}_{M_{cr}}}^2 \quad (40)$$

which is derived assuming the coefficient of variation of the sampled mean to be equal to $V_{\bar{\mu}_{M_{cr}}} = V_{M_{cr}} / \sqrt{n_{\mu_{M_{cr}}}^s}$ [15,16]. In a similar way, the required sample size for the approximation of the standard deviation with specified confidence level $C_{\sigma_{M_{cr}}}$ is obtained from

$$n_{\sigma_{M_{cr}}}^s \geq \frac{1}{2} \left(\frac{\Phi^{-1} \left(\frac{1 + C_{\sigma_{M_{cr}}}}{2} \right)}{1 - C_{\sigma_{M_{cr}}}} \right)^2 \quad (41)$$

where the coefficient of variation of the sampled standard deviation is taken as $V_{\bar{\sigma}_{M_{cr}}} = 1 / \sqrt{2n_{\sigma_{M_{cr}}}^s}$ [16].

Under the condition that the same confidence level is desired for both the mean and standard deviation, and assuming the coefficient of variation of the response to be smaller than $V_{M_{cr}} = \frac{1}{2}\sqrt{2}$, the sample size requirement is governed by Eq. (41). This sample size estimate is independent of the response and depends only on the confidence level. For a 95% confidence level of the standard deviation a sample size of 768 is required, for a confidence level of 99% this number increases to 33,174.

The advantage of the crude Monte Carlo method is that no assumptions regarding the distribution of the critical Mach number are made. Its obvious disadvantage is the computational effort it requires.

2. Perturbation Methods

The statistical moments of the flutter or divergence point can be approximated using the perturbation method [4]. This method is based on the multidimensional second-order Taylor expansion given

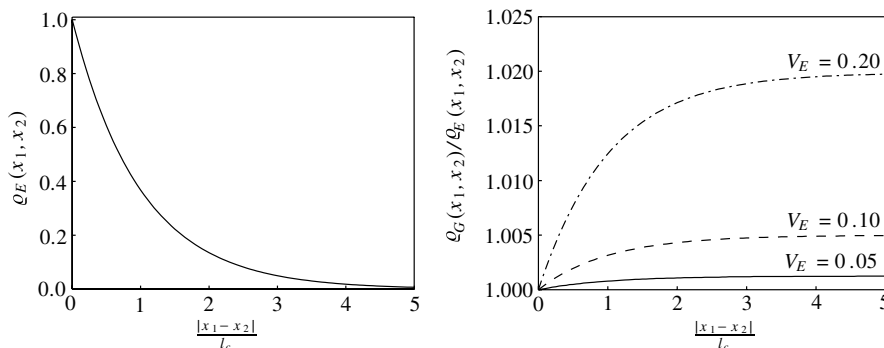


Fig. 6 Prescribed autocorrelation function (left), and ratio of correlation function for the underlying Gaussian field and prescribed autocorrelation function (right).

by

$$M_{\text{cr}}(\mathbf{z}) = M_{\text{cr}}|_{\alpha} + \nabla M_{\text{cr}}|_{\alpha}(\mathbf{z} - \alpha) + \frac{1}{2}(\mathbf{z} - \alpha)^T \nabla^{(2)} M_{\text{cr}}|_{\alpha}(\mathbf{z} - \alpha) \quad (42)$$

where $\nabla M_{\text{cr}}|_{\alpha}$ and $\nabla^{(2)} M_{\text{cr}}|_{\alpha}$ are, respectively, the gradient and Hessian of the critical Mach number with respect to the standard normal random variables, both evaluated at the center of expansion α . For notational convenience this expression is rewritten as

$$M_{\text{cr}}(\mathbf{z}) = a + \mathbf{b}^T \mathbf{z} + \frac{1}{2} \mathbf{z}^T \mathbf{C} \mathbf{z} \quad (43)$$

with

$$a = M_{\text{cr}}|_{\alpha} - \nabla M_{\text{cr}}|_{\alpha} \alpha + \frac{1}{2} \alpha^T \nabla^{(2)} M_{\text{cr}}|_{\alpha} \alpha \quad (44)$$

$$\mathbf{b}^T = \nabla M_{\text{cr}}|_{\alpha} - \alpha^T \nabla^{(2)} M_{\text{cr}}|_{\alpha} \quad (45)$$

$$\mathbf{C} = \nabla^{(2)} M_{\text{cr}}|_{\alpha} \quad (46)$$

The mean critical point is obtained by using the quadratic expansion in Eq. (43) as [17]

$$\mu_{M_{\text{cr}}} = \int_{\mathbb{R}^m} M_{\text{cr}}(\mathbf{z}) p_{\mathbf{z}} d\mathbf{z} = a + \frac{1}{2} \text{Tr}[\mathbf{C}] \quad (47)$$

Similarly, the variance of the critical Mach number is obtained as

$$\sigma_{M_{\text{cr}}}^2 = \int_{\mathbb{R}^m} (M_{\text{cr}}(\mathbf{z}) - \mu_{M_{\text{cr}}})^2 p_{\mathbf{z}} d\mathbf{z} = \mathbf{b}^T \mathbf{b} + \frac{1}{2} \text{Tr}[\mathbf{C}^2] \quad (48)$$

Remark 3: The expressions for the mean and standard deviation of the critical point in terms of its sensitivities are based on the fact that uncorrelated standard normal random variables are considered (i.e., the correlation matrix is equal to the identity matrix). For that reason, the expressions deviate from those commonly used for the perturbation method [4]. It is important to note that for the second-order expression of the mean, only the diagonal entries of the Hessian are required, which saves computational effort. Unfortunately all entries of the Hessian are required for the second-order standard deviation.

Obviously, the quality of the approximated statistical moments depends on the choice for the center of expansion α . In the case that the input random field is Gaussian, a simple choice is to use $\alpha = \mathbf{0}$. This choice implies an expansion around the mean of the input random field and is therefore referred to as the mean-centered perturbation method. For a normal distribution, the mean coincides with the median and the mode of the considered field. For the lognormal random field considered here, the mean, median, and mode do not coincide. Therefore, mean-centered, median-centered,

and mode-centered perturbation methods are used, as described in the following:

1) The choice of α for the *mean-centered perturbation method* is obtained by requiring the random field in Eq. (37) to be equal to the mean at every point on the plate

$$\mu_E = \frac{\mu_E}{\sqrt{1 + V_E^2}} \prod_{i=1}^m \exp(\sqrt{\zeta_i} \hat{r}_i(x) \alpha_i^{\text{mean}}), \quad \forall x \in [0, h] \quad (49)$$

In its strong form, this requirement can only be satisfied for each point as $m \rightarrow \infty$. Instead, we enforce the condition weakly. This is done by first rewriting Eq. (49) to yield

$$\frac{1}{2} \ln(1 + V_E^2) = \sum_{i=1}^m \sqrt{\zeta_i} \hat{r}_i(x) \alpha_i^{\text{mean}} \quad (50)$$

and then projecting it on the basis of Karhunen–Loeve functions $\hat{r}_i(x)$ using

$$\int_{-\frac{h}{2}}^{\frac{h}{2}} \frac{1}{2} \ln(1 + V_E^2) \hat{r}_j(x) dx = \int_{-\frac{h}{2}}^{\frac{h}{2}} \sum_{i=1}^m \sqrt{\zeta_i} \hat{r}_i(x) \alpha_i^{\text{mean}} \hat{r}_j(x) dx \quad (51)$$

for $j = 1, \dots, m$. Using the orthogonality of the Karhunen–Loeve functions, the components of α^{mean} are obtained as

$$\alpha_i^{\text{mean}} = \frac{1}{2} \ln(1 + V_E^2) \frac{\int_{-\frac{h}{2}}^{\frac{h}{2}} \hat{r}_i(x) dx}{\sqrt{\zeta_i}} \quad \text{for } i = 1, \dots, m \quad (52)$$

The realization of the random field in Eq. (37) for $\mathbf{z} = \alpha^{\text{mean}}$ is shown in Fig. 7. The relative error of the mean remains smaller than approximately 0.2%.

2) For the *median-centered perturbation method*, α is chosen such that the lognormal random field in Eq. (37) is equal to the median of the lognormal distribution

$$\text{Med}[\tilde{E}(x)] = \frac{\mu_E}{\sqrt{1 + V_E^2}} = E(x, \alpha^{\text{med}}) \quad \forall x \in [0, h] \quad (53)$$

The components are obtained in the same way as for the mean-centered perturbation method, which results in

$$\alpha_i^{\text{med}} = 0 \quad \text{for } i = 1, \dots, m \quad (54)$$

This result coincides with the corresponding perturbation method for a normal input random field, which could be expected because the cumulative density function is preserved upon the transformation in Eq. (33). In Fig. 7 it can be seen that the realization of the random field in Eq. (37) for $\mathbf{z} = \alpha^{\text{med}}$ exactly equals the median in all points.

3) For the *mode-centered perturbation method*, α is selected to resemble the mode of the lognormal field in Eq. (37) given by

$$\text{Mod}[\tilde{E}(x)] = \frac{\mu_E}{(1 + V_E^2)^{\frac{1}{2}}} = E(x, \alpha^{\text{mod}}) \quad \forall x \in [0, h] \quad (55)$$

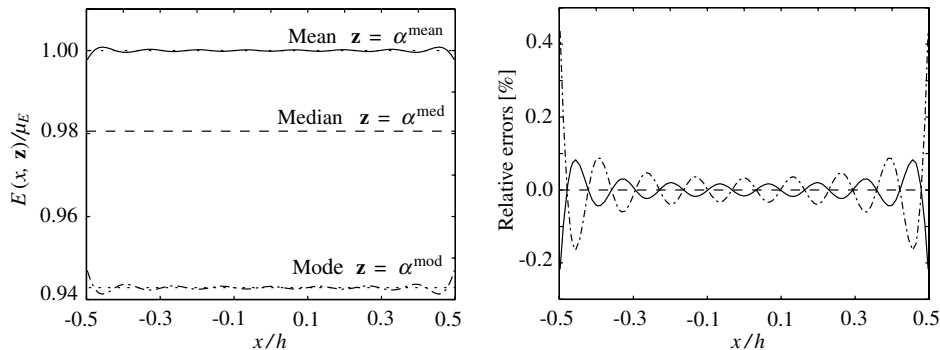


Fig. 7 Realizations and relative errors of the lognormal random field for the expansion point corresponding to the mean (solid), median (dashed), and mode (dash-dot) compared with the exact quantities (dotted). This plot is based on the discretization parameters as mentioned in Sec. V, with coefficient of variation $V_E = 0.2$.

The components are obtained in the same way as for the mean-centered perturbation method, which results in

$$\alpha_i^{\text{mod}} = -\ell_n(1 + V_E^2) \frac{\int_{-\frac{\ell}{2}}^{\frac{\ell}{2}} \hat{\gamma}_i(x) dx}{\sqrt{\xi_i}} \quad \text{for } i = 1, \dots, m \quad (56)$$

The realization of the random field in Eq. (37) for $\mathbf{z} = \boldsymbol{\alpha}^{\text{mod}}$ is shown in Fig. 7. The relative error of the mode remains smaller than approximately 0.5%.

C. Reliability Analysis

The statistical moments of the critical Mach number give an indication of the sensitivity of the problem to the random input field. However, from a design point of view it is often of more interest to investigate the occurrence of a rare event, in this case the occurrence of flutter or divergence below a specified Mach number M_{lim} . Because the occurrence of either flutter or divergence will lead to failure, the probability of failure p_{fail} can be expressed mathematically as

$$p_{\text{fail}} = \Pr[M_{\text{cr}}(\tilde{\mathbf{z}}) < M_{\text{lim}}] = \int_{\mathbb{R}^m} \mathcal{I}(\mathbf{z}) \varphi(\mathbf{z}) d\mathbf{z} \quad (57)$$

where the indicator function $\mathcal{I}(\tilde{\mathbf{z}})$ is defined as

$$\mathcal{I}(\tilde{\mathbf{z}}) = \begin{cases} 1 & M_{\text{cr}}(\tilde{\mathbf{z}}) < M_{\text{lim}} \\ 0 & M_{\text{cr}}(\tilde{\mathbf{z}}) \geq M_{\text{lim}} \end{cases} \quad (58)$$

As illustrated in Fig. 8, the random space is divided in two parts by the limit-state function

$$G(\tilde{\mathbf{z}}) = M_{\text{cr}}(\tilde{\mathbf{z}}) - M_{\text{lim}} = 0 \quad (59)$$

It is assumed that the “safe” domain ($G(\tilde{\mathbf{z}}) > 0$) and “failure” domain ($G(\tilde{\mathbf{z}}) \leq 0$) are connected domains and that the curvature of the limit-state function is relatively small. The appropriateness of these assumptions will be demonstrated by numerical experiments.

Three methods are considered for the computation of the probability of failure: the sampling-based crude Monte-Carlo method, the sensitivity-based geometrical reliability method, and the importance sampling method, which can be seen as a combination of the first two methods.

1. Crude Monte Carlo Method

For the crude Monte Carlo method, the probability of failure in Eq. (57) is approximated as

$$\bar{p}_{\text{fail}} = \frac{1}{n_{\text{pfail}}^s} \sum_{i=1}^{n_{\text{pfail}}^s} \mathcal{I}(\mathbf{z}_i) \quad (60)$$

where the required sample size n_{pfail}^s depends on the required confidence level

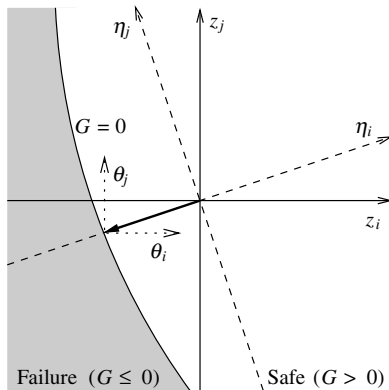


Fig. 8 Schematic representation of the random space.

$$\Pr\left[\left|\frac{\bar{p}_{\text{fail}} - p_{\text{fail}}}{p_{\text{fail}}}\right| \geq 1 - C_{p_{\text{fail}}}\right] \leq 1 - C_{p_{\text{fail}}} \quad (61)$$

Because the probability of failure is defined as the mean of the indicator function in Eq. (58), Eq. (40) can be rewritten to yield

$$n_{\text{pfail}}^s \geq \left(\frac{\Phi^{-1}\left(\frac{1+C_{p_{\text{fail}}}}{2}\right)}{1 - C_{p_{\text{fail}}}}\right)^2 V_{\tilde{\mathbf{z}}}^2 \quad (62)$$

where the square of the coefficient of variation of the indicator function is given by

$$V_{\tilde{\mathbf{z}}}^2 = \frac{E[\tilde{\mathbf{z}}^2] - \mu_{\tilde{\mathbf{z}}}^2}{\mu_{\tilde{\mathbf{z}}}^2} = \frac{1}{p_{\text{fail}}} - 1 \quad (63)$$

Equations (62) and (63) demonstrate that the required sample size primarily depends on the probability of failure. Because generally rare events (very small probability of occurrence) are considered, crude Monte Carlo sampling requires large sample sizes and is therefore very computationally intensive.

2. Geometrical Reliability Method

In the reliability method, the limit-state function in Eq. (59) is approximated by a Taylor expansion, which makes analytical determination of the probability of failure possible. The approximation of the limit-state function $G(\mathbf{z}) = 0$ can best be done by using a Taylor expansion around the point that is closest to the origin, where the contribution to the integral shown in Eq. (57) is largest. This point is indicated by \mathbf{z}^* and is often referred to as the design point or β point (because $\beta = \|\mathbf{z}^*\|$).

Under the assumption that the limit-state function is smooth and its curvature relatively small, the design point can be found by solving the minimization problem

$$\begin{cases} \text{minimize} & \|\mathbf{z}\| \\ \text{subject to} & M_{\text{cr}}(\mathbf{z}) = M_{\text{lim}} \end{cases} \quad (64)$$

The Hasofer–Lind Rackwitz–Fiessler algorithm [18] can be used to solve this minimization problem. This algorithm determines an improved estimate \mathbf{z}^{k+1} from a given point \mathbf{z}^k in random space using

$$\mathbf{z}^{k+1} = \frac{[\nabla M_{\text{cr}}|_{\mathbf{z}^k} \mathbf{z}^k - (M_{\text{cr}}(\mathbf{z}^k) - M_{\text{lim}})] \nabla M_{\text{cr}}|_{\mathbf{z}^k}^T}{\|\nabla M_{\text{cr}}|_{\mathbf{z}^k}\|^2} \quad (65)$$

Combining Eq. (65) with expressions for the sensitivities obtained in Sec. IV allows the design point \mathbf{z}^* to be determined iteratively.

Once the design point is computed, the probability of failure shown in Eq. (57) can be evaluated by rotation of random space as illustrated in Fig. 8. If the limit-state surface is approximated as a linear plane orthogonal to the η_1 axis, the probability of failure p_{fail} following from the first-order reliability method (FORM) is given by

$$p_{\text{fail}} = \int_{\mathbb{R}^m} \mathcal{I}(\boldsymbol{\eta}) \varphi(\boldsymbol{\eta}) d\boldsymbol{\eta} = \int_{-\infty}^{\infty} \mathcal{I}(\eta_1) \varphi(\eta_1) d\eta_1 = \Phi(-\beta) \quad (66)$$

The first-order result can be improved by application of the Breitung correction factor [19]. This is called the second-order reliability method (SORM) because the curvature of the limit-state function is also taken into account. The probability of failure is then given by

$$p_{\text{fail}} = \Phi(-\beta) \prod_{i=1}^{m-1} \frac{1}{\sqrt{1 + \beta \kappa_i}} \quad (67)$$

where $\{\kappa_i\}$ are the main curvatures of the limit-state function at the design point. The main curvatures are computed on the basis of the second-order derivatives of the critical Mach number as derived in Sec. IV.

The advantage of the geometrical reliability method is that it requires little computational effort compared with crude Monte Carlo sampling. The drawback of the method is, however, its lack of accuracy. Especially in cases with large coefficients of

variation, the reliability method tends to underestimate the probability of failure.

3. Importance Sampling

The idea of importance sampling is to use the computed design point to reduce the required sample size of the crude Monte Carlo simulation, by sampling around the design point ($\mathbf{z} = \mathbf{z}^*$) rather than around the mean of the normal random space ($\mathbf{z} = \mathbf{0}$). This is done by defining $\boldsymbol{\theta} = \mathbf{z} - \mathbf{z}^*$, such that the design point corresponds to $\boldsymbol{\theta}^* = \mathbf{0}$. The probability of failure can then be expressed as

$$p_{\text{fail}} = \int_{\mathbb{R}^m} \mathbb{I}(\boldsymbol{\theta}, \mathbf{z}^*) \varphi(\boldsymbol{\theta}) d\boldsymbol{\theta} \quad (68)$$

with \mathbb{I} being the shifted indicator function defined as

$$\mathbb{I}(\boldsymbol{\theta}, \mathbf{z}^*) = \mathcal{I}(\boldsymbol{\theta} + \mathbf{z}^*) \frac{\varphi(\boldsymbol{\theta} + \mathbf{z}^*)}{\varphi(\boldsymbol{\theta})} \quad (69)$$

From Eq. (68) it is clear that the probability of failure is equal to the mean of this shifted indicator function, which can be obtained using Monte Carlo sampling as

$$\bar{p}_{\text{fail}} = \frac{1}{n_{\mu_{\tau}}^s} \sum_{i=1}^{n_{\mu_{\tau}}^s} \mathcal{I}(\boldsymbol{\theta}_i + \mathbf{z}^*) \frac{\varphi(\boldsymbol{\theta}_i + \mathbf{z}^*)}{\varphi(\boldsymbol{\theta}_i)} \quad (70)$$

An approximation of the required sample for the computation of this probability of failure with confidence level $C_{\mu_{\tau}}$ follows from Eq. (62) as

$$n_{\mu_{\tau}}^s \geq \left(\frac{\Phi^{-1}\left(\frac{1+C_{\mu_{\tau}}}{2}\right)}{1-C_{\mu_{\tau}}}\right)^2 V_{\tau}^2 \quad (71)$$

The square of the coefficient of variation is given by

$$V_{\tau}^2 = \frac{E[\mathbb{I}^2] - p_{\text{fail}}^2}{p_{\text{fail}}^2} \quad (72)$$

with

$$E[\mathbb{I}^2] = \int_{\mathbb{R}^m} \mathcal{I}(\mathbf{z}) \frac{\varphi(\mathbf{z})}{\varphi(\boldsymbol{\theta})} \varphi(\mathbf{z}) d\mathbf{z} \quad (73)$$

In case the design point is sufficiently large ($\beta \gg 1$), this expression can be rewritten as

$$E[\mathbb{I}^2] \approx \exp\left(-\frac{1}{2}\beta^2\right) \int_{\mathbb{R}^m} \mathcal{I}(\mathbf{z}) \varphi(\mathbf{z}) d\mathbf{z} \approx 2p_{\text{fail}}^2 \quad (74)$$

Substitution of this result in Eq. (72) then yields $V_{\tau} = 1$, which can be substituted in Eq. (71) to obtain an estimate for the required sample size as

$$n_{\mu_{\tau}}^s \geq \left(\frac{\Phi^{-1}\left(\frac{1+C_{\mu_{\tau}}}{2}\right)}{1-C_{\mu_{\tau}}}\right)^2 \quad (75)$$

which is independent of the probability of failure. In contrast to the crude Monte Carlo method, importance sampling remains feasible if the probability of failure is small.

IV. Sensitivities Computation

As discussed in the previous section, the first- and second-order sensitivities of the critical points are required for various methods for uncertainty and reliability analysis. The determination of the sensitivities of the divergence point and flutter point is discussed next.

A. Sensitivities of the Divergence Point

The first-order derivatives of the divergence point $M_{\text{div}}(\tilde{\mathbf{z}})$ with respect to the random variables $\tilde{\mathbf{z}}$ can be computed by the

differentiation of Eq. (24) with respect to the random variables to obtain

$$\frac{d|\lambda_1|}{d\tilde{z}_i} = \frac{\partial|\lambda_1|}{\partial M_{\text{div}}} \frac{\partial M_{\text{div}}}{\partial \tilde{z}_i} + \frac{\partial|\lambda_1|}{\partial \tilde{z}_i} = 0 \quad \text{for } i = 1, \dots, m \quad (76)$$

Rewriting this expression yields the sensitivity of the divergence point as

$$\frac{\partial M_{\text{div}}}{\partial \tilde{z}_i} = -\left(\frac{\partial|\lambda_1|}{\partial M_{\text{div}}}\right)^{-1} \frac{\partial|\lambda_1|}{\partial \tilde{z}_i} \quad \text{for } i = 1, \dots, m \quad (77)$$

The second-order derivatives of the flutter point with respect to the random variables $\tilde{\mathbf{z}}$ is obtained by differentiating Eq. (76) with respect to $\tilde{\mathbf{z}}$ to get

$$\begin{aligned} \frac{d^2|\lambda_1|}{d\tilde{z}_i d\tilde{z}_j} &= \frac{\partial^2|\lambda_1|}{\partial M_{\text{div}}^2} \frac{\partial M_{\text{div}}}{\partial \tilde{z}_i} \frac{\partial M_{\text{div}}}{\partial \tilde{z}_j} + \frac{\partial^2|\lambda_1|}{\partial M_{\text{div}} \partial \tilde{z}_j} \frac{\partial M_{\text{div}}}{\partial \tilde{z}_i} + \frac{\partial^2|\lambda_1|}{\partial M_{\text{div}} \partial \tilde{z}_i} \frac{\partial M_{\text{div}}}{\partial \tilde{z}_j} \\ &+ \frac{\partial|\lambda_1|}{\partial M_{\text{div}}} \frac{\partial^2 M_{\text{div}}}{\partial \tilde{z}_i \partial \tilde{z}_j} + \frac{\partial^2|\lambda_1|}{\partial \tilde{z}_i \partial \tilde{z}_j} = 0 \quad \text{for } i, j = 1, \dots, m \end{aligned} \quad (78)$$

Rewriting this expression then yields the second-order sensitivities of the divergence point as

$$\begin{aligned} \frac{\partial^2 M_{\text{div}}}{\partial \tilde{z}_i \partial \tilde{z}_j} &= -\left(\frac{\partial|\lambda_1|}{\partial M_{\text{div}}}\right)^{-1} \left[\frac{\partial^2|\lambda_1|}{\partial M_{\text{div}}^2} \frac{\partial M_{\text{div}}}{\partial \tilde{z}_i} \frac{\partial M_{\text{div}}}{\partial \tilde{z}_j} + \frac{\partial^2|\lambda_1|}{\partial M_{\text{div}} \partial \tilde{z}_j} \frac{\partial M_{\text{div}}}{\partial \tilde{z}_i} \right. \\ &\left. + \frac{\partial^2|\lambda_1|}{\partial M_{\text{div}} \partial \tilde{z}_i} \frac{\partial M_{\text{div}}}{\partial \tilde{z}_j} + \frac{\partial^2|\lambda_1|}{\partial \tilde{z}_i \partial \tilde{z}_j} \right] \quad \text{for } i, j = 1, \dots, m \end{aligned} \quad (79)$$

From Eqs. (77) and (79) it is observed that the first- and second-order derivatives of the divergence point can be computed once the derivatives of the smallest eigenvalue λ_1 with respect to the Mach number and random variables are known. To find the eigenvalue sensitivities, the derivatives of the system matrices are required. These sensitivities can be obtained as explained in Sec. IV.C. Using the system matrix sensitivities, the eigenvalue derivatives are computed as elaborated in [20]. This requires the computation of the left and right eigenvector as well as the computation of the derivatives of the right eigenvector corresponding to the smallest eigenvalue. Because only the derivatives of this single eigenvector are required, Nelson's method [21] is used. This method only requires the solution of two linear systems per eigenvector derivative and can therefore efficiently be applied in this case.

B. Sensitivities of the Flutter Point

Because both the Mach number M_{∞} and random variables $\tilde{\mathbf{z}}$ are real valued, the sensitivities of the flutter point can be derived in exactly the same way as in the case of the divergence point, yielding

$$\frac{\partial M_{\Pi}}{\partial \tilde{z}_i} = -\left(\frac{\partial \delta_1}{\partial M_{\Pi}}\right)^{-1} \frac{\partial \delta_1}{\partial \tilde{z}_i} \quad \text{for } i = 1, \dots, m \quad (80)$$

and

$$\begin{aligned} \frac{\partial^2 M_{\Pi}}{\partial \tilde{z}_i \partial \tilde{z}_j} &= -\left(\frac{\partial \delta_1}{\partial M_{\Pi}}\right)^{-1} \left[\frac{\partial^2 \delta_1}{\partial M_{\Pi}^2} \frac{\partial M_{\Pi}}{\partial \tilde{z}_i} \frac{\partial M_{\Pi}}{\partial \tilde{z}_j} + \frac{\partial^2 \delta_1}{\partial M_{\Pi} \partial \tilde{z}_j} \frac{\partial M_{\Pi}}{\partial \tilde{z}_i} \right. \\ &\left. + \frac{\partial^2 \delta_1}{\partial M_{\Pi} \partial \tilde{z}_i} \frac{\partial M_{\Pi}}{\partial \tilde{z}_j} + \frac{\partial^2 \delta_1}{\partial \tilde{z}_i \partial \tilde{z}_j} \right] \end{aligned} \quad (81)$$

The required first- and second-order derivatives of the eigenvalues are obtained as elaborated in Ref. [22] using the system matrix sensitivities as discussed in Sec. IV.C. Determination of these sensitivities requires the same operations as in the case of divergence. Two eigenvalue problems with the size of two times the number of degrees of freedom are solved and two systems of the size of the number of degrees of freedom are solved for the computation of each of the eigenvector derivatives.

C. Sensitivities of the Coupled System Matrices

To obtain the eigenvalue sensitivities, the derivatives of the system matrices with respect to the random variables are required. Because the randomness is considered to be in the modulus of elasticity alone, the mass and damping matrix are not random. The stiffness matrix of the coupled system is random and its sensitivities are obtained as

$$\frac{\partial \tilde{\mathbf{K}}}{\partial \tilde{z}_i} = \frac{\partial \mathbf{K}}{\partial \tilde{E}} \frac{\partial \tilde{E}}{\partial \tilde{z}_i} \quad \text{and} \quad \frac{\partial^2 \tilde{\mathbf{K}}}{\partial \tilde{z}_i \partial \tilde{z}_j} = \frac{\partial \mathbf{K}}{\partial \tilde{E}} \frac{\partial^2 \tilde{E}}{\partial \tilde{z}_i \partial \tilde{z}_j} + \frac{\partial^2 \mathbf{K}}{\partial \tilde{E}^2} \frac{\partial \tilde{E}}{\partial \tilde{z}_i} \frac{\partial \tilde{E}}{\partial \tilde{z}_j} \quad (82)$$

for $i, j = 1, \dots, m$, where the first-order and second-order derivatives of the modulus of elasticity with respect to the Gaussian random variables $\tilde{\mathbf{z}}$ are obtained by differentiation of Eq. (37) as

$$\begin{aligned} \frac{\partial E(\mathbf{x}, \mathbf{z})}{\partial \tilde{z}_i} &= \sqrt{\zeta_i} \hat{r}_i(\mathbf{x}) E(\mathbf{x}, \mathbf{z}) \quad \text{and} \\ \frac{\partial^2 E(\mathbf{x}, \mathbf{z})}{\partial \tilde{z}_i \partial \tilde{z}_j} &= \sqrt{\zeta_i \zeta_j} \hat{r}_i(\mathbf{x}) \hat{r}_j(\mathbf{x}) E(\mathbf{x}, \mathbf{z}) \end{aligned} \quad (83)$$

for $i, j = 1, \dots, m$.

V. Numerical Simulations

Numerical experiments are performed to test the proposed methods for reliability and uncertainty analysis of the critical points. All computations are performed on a 321×193 grid, for which relative errors in the deterministic critical Mach numbers of 6.6×10^{-4} and 1.5×10^{-3} were observed for divergence and flutter, respectively. The choice of this grid is dictated by the computational cost required for crude Monte Carlo simulations with acceptable confidence levels. In the subsequent sections, the results of the various methods are compared on the basis of both accuracy and computational effort. To compare the accuracy of the various methods, error estimates are obtained for both discretization errors and sampling errors.

The parameters used for the numerical simulations are assembled in Table 2. The mean modulus of elasticity μ_E is considered to be equal to the deterministic Young's modulus E as given in the parameter table. The random field for the modulus of elasticity in Eq. (37) is defined with the autocorrelation function $\rho_E = \exp(-|x_1 - x_2|/l_c)$, where the characteristic length l_c is 10% of the plate length. The plate is discretized using 16 Karhunen–Loeve terms ($m = 16$), which corresponds to the criterion that the Karhunen–Loeve expansion is truncated for eigenvalues smaller in magnitude than 5% of the largest eigenvalue magnitude. Coefficients of variation V_E up to 50% are considered.

A. Panel Divergence in Subsonic Flow

The various stochastic methods are tested for the subsonic test case introduced in Sec. II.E.1. The results for the uncertainty analyses are collected in Table 3.

The Monte Carlo simulations have been performed with a sample size of over 33,000, which is based on a confidence level of 99% for the standard deviation in the absence of discretization errors. As mentioned in Sec. II.E.1, the computation of a single realization takes about 50 s on a 2.8 GHz Quad-Core Intel Xeon 5400 series processor. Because the crude Monte Carlo method is suitable for parallel computing, a computation can be performed in less than three days on a platform with two of the previously mentioned processors (8 cores) and 10 GB of internal memory. Assessment of the discretization error in a Monte Carlo simulation is a delicate task. The main problem is that the discretization error is, in general, dependent on the realization considered and is therefore a random variable. As outlined in the Appendix, this random error reduces the overall confidence level. Information about these confidence levels is incorporated in Table 3. The confidence levels for both the mean and standard deviation are hardly affected by the discretization error.

Computation of the statistical moments using the perturbation methods on the 321×193 grid requires 32 min, which is 38 times the deterministic computation time. In contrast to the crude Monte Carlo

Table 3 Results of the methods for uncertainty analysis for the divergence test case with a grid of 321×193 points. The deterministic divergence Mach number is $M_{\text{div}} = 0.149$.^a

	Mean $\mu_{M_{\text{div}}}$		
	0.10	0.25	0.50
V_E			
Crude Monte Carlo	0.148 (9.1×10^{-4})	0.146 (1.7×10^{-3})	0.139 (2.5×10^{-3})
Mean centered	0.148 (6.6×10^{-4})	0.146 (6.7×10^{-4})	0.139 (6.9×10^{-4})
Median centered	0.148 (6.6×10^{-4})	0.146 (6.7×10^{-4})	0.139 (6.9×10^{-4})
Mode centered	0.148 (6.6×10^{-4})	0.146 (6.7×10^{-4})	0.139 (6.9×10^{-4})
	Standard deviation $\sigma_{M_{\text{div}}}$		
	0.10	0.25	0.50
V_E			
Crude Monte Carlo	0.0032 (1.1×10^{-2})	0.0079 (1.1×10^{-2})	0.015 (1.1×10^{-2})
Mean centered	0.00324 (6.7×10^{-4})	0.00796 (6.6×10^{-4})	0.0151 (6.5×10^{-4})
Median centered	0.00324 (6.7×10^{-4})	0.00796 (6.6×10^{-4})	0.0151 (6.5×10^{-4})
Mode centered	0.00324 (6.7×10^{-4})	0.00795 (6.6×10^{-4})	0.0149 (6.5×10^{-4})

method, an error estimate of the results for the perturbation methods can be obtained in a straight forward manner by means of a mesh convergence study. The discretization errors for the mean and standard deviation are defined as

$$\begin{aligned} \epsilon_{\mu_{M_{\text{cr}}}} &= \frac{\mu_{M_{\text{cr}}}(\Delta) - \mu_{M_{\text{cr}}}(\Delta_{\text{res}})}{\mu_{M_{\text{cr}}}(\Delta_{\text{res}})} \quad \text{and} \\ \epsilon_{\sigma_{M_{\text{cr}}}} &= \frac{\sigma_{M_{\text{cr}}}(\Delta) - \sigma_{M_{\text{cr}}}(\Delta_{\text{res}})}{\sigma_{M_{\text{cr}}}(\Delta_{\text{res}})} \end{aligned} \quad (84)$$

respectively, with Δ_{res} being the mesh size corresponding to the 641×385 grid. In Fig. 9 the relative errors are plotted for various grid sizes for the mean-centered perturbation method with 10% coefficient of variation in the modulus of elasticity. As can be seen, the 321×193 grid result falls in the asymptotic region of convergence. The relative errors of the mean and standard deviation on this grid are respectively 6.6×10^{-4} cos and 6.7×10^{-4} , both of which hardly differ from the deterministic error $\epsilon_{M_{\text{cr}}} = 6.6 \times 10^{-4}$. For all other simulations, the relative errors are collected in Table 3. As can be seen, all errors in the mean and standard deviation remain of the same order of magnitude as the deterministic error.

The results of all the perturbation methods are in excellent agreement with those obtained using the crude Monte Carlo simulation. Apparently, the relation between the divergence point and the random variable can very well be approximated by a second-order Taylor expansion. Because accurate perturbation results are obtained with only a small fraction of the computational effort involved in crude Monte Carlo sampling, the perturbation method is considered to be more efficient than the crude Monte Carlo method in the considered test case.

A significant drop of the mean divergence point is observed. In the case of 25% coefficient of variation of the modulus of elasticity, the mean drops with 1.7%. In the case of $V_E = 50\%$, a drop of 6% is observed. The assumed uncertainties reduce the critical Mach number and hence the deterministic results are nonconservative. This effect must normally be accounted for by ad hoc safety factors. Reliability analysis, however, can be used for the more precise definition of these safety factors.

The results of the methods for reliability analysis are compared in Table 4, where the probability of the occurrence of divergence below a Mach number of 0.125 is considered.

The sample obtained for uncertainty analysis is used to obtain the crude Monte Carlo reliability results. In the absence of a discretization error, the confidence levels are obtained using Eq. (A8)

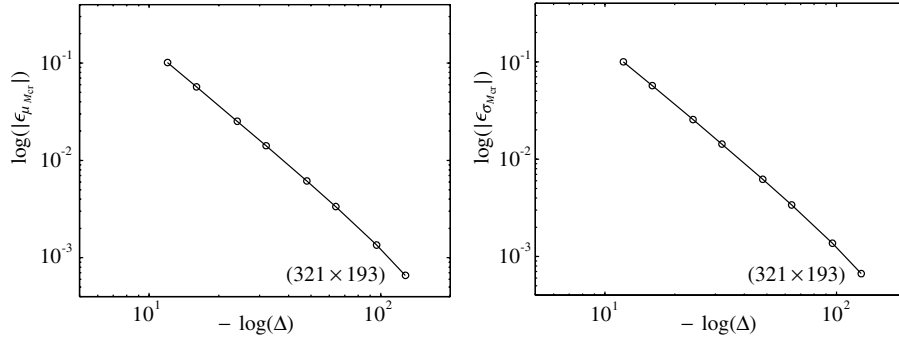


Fig. 9 Mesh convergence plots of the mean (left) and standard deviation (right) of the critical Mach number for subsonic divergence. The errors are defined in Eq. (84). The solution on a 641×385 Cartesian grid is considered as the fully resolved solution.

as 97.1 and 83.4% for the cases of 50 and 25% coefficient of variation of the modulus of elasticity. The probability of failure with 10% variation in the Young's modulus cannot be determined, because the probability is too small to be computed using 33,000 realizations. The influence of the discretization error on the confidence level is described in the Appendix. The confidence levels, including the influence of the random discretization errors, are incorporated in Table 4.

The computation of the probability of failure on the 321×193 grid using the reliability methods takes approximately 80 min on the previously mentioned hardware. An error estimate of the results can be obtained by means of a mesh convergence study. The discretization error

$$\epsilon_{p_{\text{fail}}}(\Delta) = \frac{p_{\text{fail}}(\Delta) - p_{\text{fail}}(\Delta_{\text{res}})}{p_{\text{fail}}(\Delta_{\text{res}})} \quad (85)$$

is shown in Fig. 9 for the first-order reliability method results corresponding to 25% coefficient of variation in the modulus of elasticity. As can be seen, the 321×193 falls in the asymptotic region of convergence. The relative error of the failure probability is -1.0×10^{-2} . The corresponding relative error in the design point is given by

$$\epsilon_{\beta}(\Delta) = \frac{p_{\text{fail}}(\Delta_{\text{res}})}{\beta(\Delta_{\text{res}})\varphi(\beta(\Delta_{\text{res}}))} \epsilon_{p_{\text{fail}}}(\Delta) \quad (86)$$

which equals -5.6×10^{-3} and falls in the asymptotic region of convergence. For the performed simulations it is observed that this relative error in the beta point remains of the same order of magnitude upon changing the coefficient of variation of the modulus of elasticity. Consequently, the relative error in the probability of failure increases significantly upon decreasing the failure probability. As can be seen in Table 4, the relative error of the failure probability increases to 21% for the case of 10% coefficient of variation in the Young's modulus.

The importance sampling simulations are performed using over 15,000 realizations, which corresponds with a confidence level of 95%. These simulations take less than half the time of the considered crude Monte Carlo simulations. The confidence levels with the

discretization error incorporated are shown in Table 4. As can be seen, the confidence levels for the two smallest failure probabilities are considerably better than in the crude Monte Carlo case, despite the fact that less than half of the numbers of realizations are used. For the relatively large failure probability corresponding to a 50% modulus of elasticity coefficient of variation, a comparable confidence level is achieved as in the crude Monte Carlo case.

As can be seen in Table 4, the importance sampling method and crude Monte Carlo method both converge to the same probabilities of failure, which implies that the assumptions made for the importance sampling method are valid. For the same reason, the importance sampling results can also be used as a benchmark. As can be seen, the first- and second-order reliability methods give reasonable estimates for the probability of failure. For the performed simulations, SORM turns out to be an appropriate method, because its computational cost is negligible compared with the importance sampling method.

B. Panel Flutter in Supersonic Flow

The results of the uncertainty analyses for the flutter test case as introduced in Sec. II.E.2 are assembled in Table 5, and the results of the reliability analyses are presented in Table 6. As in the divergence test case, the crude Monte Carlo results (for both uncertainty and reliability analysis) are based on a simulation with over 33,000 realizations. The corresponding confidence levels, in which the influence of the discretization errors is incorporated, are collected in the tables. With a computation time of approximately 150 s per realization, the total computation time of the crude parallelized Monte Carlo method on the already mentioned hardware is just over

Table 5 Results of the methods for uncertainty analysis for the divergence test case, with a grid of 321×193 points. The deterministic flutter Mach number is $M_{\text{fl}} = 2.27$.^a

	Mean $\mu_{M_{\text{fl}}}$	
	0.10	0.25
V_E	0.10	0.25
Crude Monte Carlo	2.25 (2.6×10^{-3})	2.13 (4.1×10^{-3})
Mean centered	2.25 (1.5×10^{-3})	2.16 (1.5×10^{-3})
Median centered	2.25 (1.5×10^{-3})	2.16 (1.5×10^{-3})
Mode centered	2.25 (1.5×10^{-3})	2.14 (1.3×10^{-3})
Standard deviation $\sigma_{M_{\text{fl}}}$		
V_E	0.10	0.25
Crude Monte Carlo	0.14 (1.6×10^{-2})	0.36 (1.5×10^{-2})
Mean centered	0.135 (5.1×10^{-3})	0.334 (4.9×10^{-3})
Median centered	0.135 (5.1×10^{-3})	0.335 (4.9×10^{-3})
Mode centered	0.135 (5.1×10^{-3})	0.327 (4.4×10^{-3})

Table 4 Results of the methods for reliability analysis for the divergence test case, with $M_{\text{lim}} = 0.125$.^b

	Failure probability p_{fail}		
	0.10	0.25	0.50
V_E	0.10	0.25	0.50
Crude Monte Carlo		0.0023 (2.0×10^{-1})	0.17 (3.9×10^{-2})
FORM	3.5×10^{-15} (-2.1×10^{-1})	0.0018 (-3.8×10^{-2})	0.13 (-1.0×10^{-2})
SORM	4.2×10^{-15} (-2.1×10^{-1})	0.0021 (-3.8×10^{-2})	0.15 (-9.7×10^{-3})
Importance sampling	4.7×10^{-15} (2.5×10^{-1})	0.0024 (8.7×10^{-2})	0.17 (5.9×10^{-2})

Table 6 Results of the methods for reliability analysis for the divergence test case, with $M_{lim} = 1.75$.^b

	p_{fail}	
V_E	0.10	0.25
Crude Monte Carlo		0.13 (8.4×10^{-2})
FORM	1.6×10^{-4} (-1.4×10^{-2})	0.11 (-2.4×10^{-3})
SORM	3.7×10^{-4} (1.0×10^{-1})	0.20 (6.1×10^{-2})
Importance sampling	1.8×10^{-4} (6.3×10^{-2})	0.13 (5.2×10^{-2})

^aFor the perturbation methods, the relative errors as defined in Eq. (84) are indicated in between the brackets. For the crude Monte Carlo method, one minus the confidence level (as defined in the Appendix) is shown.

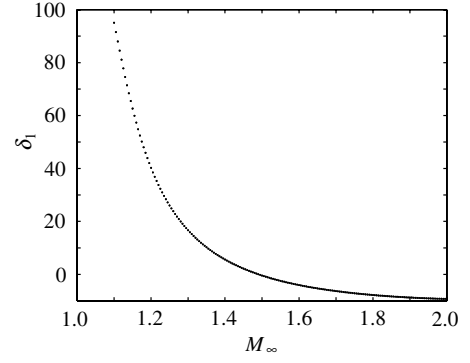
^bFor the reliability methods, the relative errors as defined in Eq. (85) are indicated in between the brackets. For the crude Monte Carlo method and importance sampling method, one minus the confidence level (as defined in the Appendix) is shown.

7 days. The discretization errors of the perturbation methods and reliability methods are, as in the subsonic case, estimated using a mesh convergence study. The resulting errors are presented in Fig. 10 and Tables 5 and 6. The importance sampling simulations are performed with a confidence level of 95%, requiring a sample size of over 15,000. As can be seen in Table 6, the confidence levels achieved by this importance sampling simulation are considerably better than these for the crude Monte Carlo method, despite the fact that less than half of the computational effort is required.

As can be seen in Table 5, the mean and standard deviation are accurately predicted by the perturbation methods in the case of 10% coefficient of variation in the modulus of elasticity. In the case of 25% coefficient of variation, the mean is overestimated by the perturbation methods, especially by the mean-centered and median-centered perturbation methods. The mode-centered method gives the best correspondence with the crude Monte Carlo result. The standard deviation is underestimated by all perturbation methods. This increased error can (at least partially) be explained by the behavior of the fluid model near the sonic speed ($M_\infty = 1$). As can be seen in Fig. 11, the real part of the smallest eigenvalue approaches an asymptote at that speed. As a consequence, the second-order truncation of the Taylor expansion of the response yields inaccurate approximations. According to the results of the reliability analysis, there is a significant contribution of this regime to the statistical moments because, on average, approximately 1 out of every 8 realizations falls in the regime below $M_\infty = 1.75$. Approximately 1 out of every 16 realizations even falls in the regime below $M_\infty = 1.50$.

As in the case of divergence, the mean critical Mach number drops due to the uncertainties in the modulus of elasticity. For 25% coefficient of variation, the mean drops with 6.2%. Hence, the influence of the uncertainties is much stronger in the flutter case. This is confirmed by the fact that the coefficient of variation of the flutter point is considerably larger than that of the divergence point (16.9 vs 5.4% for the case of 25% Young's modulus coefficient of variation).

As in the divergence test case, the importance sampling method and crude Monte Carlo method produce the same results when the failure probability is relatively high ($V_E = 0.25$). Importance

**Fig. 11 Real part of the smallest eigenvalue δ_1 vs the freestream Mach number M_∞ in the transonic regime for the flutter test case.**

sampling requires, however, a smaller sample size and remains applicable for small probabilities of failure ($V_E = 0.10$). The first-order reliability method slightly underestimates the failure probability, whereas it is considerably overestimated by the second-order method. Both methods yield good indications of the failure probabilities and require negligible computation time compared with the sampling-based methods. Because SORM provides a conservative estimate of the failure probability, it is a good alternative for the sampling-based methods. If accurate results are required, importance sampling is the most attractive method.

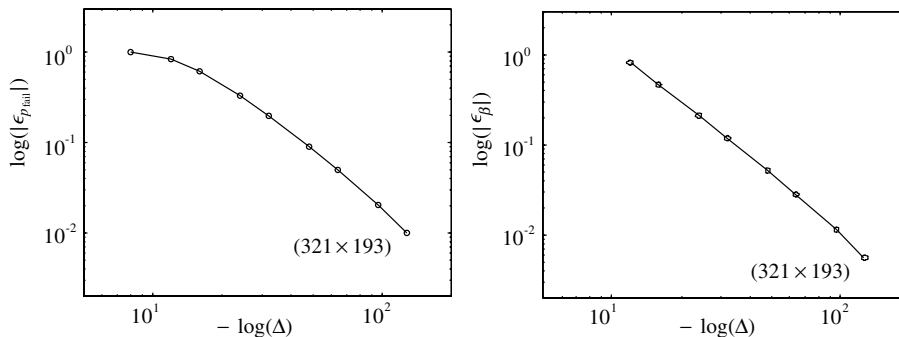
VI. Conclusions

As an example of a fluid–structure interaction model, we have considered the interaction of a flexible panel and a linearized potential flow, where the elastic properties of the panel are described using a discrete random field. The critical points and their sensitivities are obtained by consideration of the eigenvalues of a monolithically coupled system of equations.

Two methods for the determination of the statistical moments of the critical points are proposed. The crude Monte Carlo method is impractical due to the computational effort required for the computation of accurate results. For the cases considered here, the perturbation method is found to be efficient for determination of the mean and standard deviation of the critical Mach numbers. The critical points can be approximated accurately in only a small fraction of the time required for an accurate crude Monte Carlo simulation.

The probability of the occurrence of instabilities below a specified Mach number is also computed using three methods. The crude Monte Carlo method is impractical for small failure probabilities due to the required sample sizes. The sensitivity-based geometrical reliability method is found to be a good method for obtaining a reasonably accurate estimation of the failure probability. The importance sampling method can be used to increase the accuracy of the reliability method.

The results presented illustrate that the uncertainties decrease the average Mach numbers at which instabilities occur. This implies that deterministic computations yield nonconservative estimates of the

**Fig. 10 Mesh convergence plots of the probability of failure (left) and beta point (right) for subsonic divergence. The errors are defined in Eq. (85). The solution on a 641×385 Cartesian grid is considered as the fully resolved solution.**

stability boundaries. The use of stochastic methods can therefore provide critical information for the design of structures for which fluid–structure interactions are important. This contribution has demonstrated that stochastic finite element methods are practical methods for including the effect of uncertainties in realistic fluid–structure interaction problems.

Appendix: Definition of Confidence Levels for the Sampling-Based Results with Discretization Error

As outlined in Sec. V, comparison of the various methods requires a proper error analysis. The error of the sampling-based methods comprises two parts: the sampling error and the discretization error. The sampling error is controlled using a requirement for the sample sizes in Eqs. (40), (41), (62), and (75), which depend on the desired confidence levels. These confidence levels are based on the assumption of a zero discretization error. The confidence level for the mean can therefore be written as

$$\Pr \left[\left| \frac{\bar{\mu}_{M_{cr}}(\Delta_{res}) - \mu_{M_{cr}}(\Delta_{res})}{\mu_{M_{cr}}(\Delta_{res})} \right| \geq 1 - C_{\mu_{M_{cr}}} \right] \leq 1 - C_{\mu_{M_{cr}}} \quad (A1)$$

with Δ_{res} being the grid spacing at the fully resolved scale. The sampled mean, in this work, obtained on a grid with a larger grid distance Δ , such that the confidence level should be written as

$$\Pr \left[\left| \frac{\bar{\mu}_{M_{cr}}(\Delta) - \mu_{M_{cr}}(\Delta_{res})}{\mu_{M_{cr}}(\Delta_{res})} \right| \geq 1 - C_{\mu_{M_{cr}}}^* \right] \leq 1 - C_{\mu_{M_{cr}}}^* \quad (A2)$$

where the superscript star is used to indicate that a confidence level with finite discretization error is concerned. A conservative estimate of this confidence level $C_{\mu_{M_{cr}}}^*$ is obtained by equating the probabilities in Eqs. (A1) and (A2) to yield

$$C_{\mu_{M_{cr}}}^* = 1 - \left| \frac{\mu_{M_{cr}}(\Delta) - \mu_{M_{cr}}(\Delta_{res})}{\mu_{M_{cr}}(\Delta_{res})} \right| - (1 - C_{\mu_{M_{cr}}}) \frac{\sigma_{M_{cr}}(\Delta)}{\sigma_{M_{cr}}(\Delta_{res})} \quad (A3)$$

As observed from this expression, the confidence level with discretization error incorporated depends on the statistical moments of the critical Mach number on the resolved scale. For the purpose of determining the confidence level $C_{\mu_{M_{cr}}}^*$ these statistical moments are approximated using the perturbation method. In that case, the errors defined in Eq. (84) can be used to rewrite the preceding expression as

$$C_{\mu_{M_{cr}}}^* = 1 - |\epsilon_{\mu_{M_{cr}}}(\Delta)| - (1 - C_{\mu_{M_{cr}}})(1 + \epsilon_{\sigma_{M_{cr}}}(\Delta)) \quad (A4)$$

Similarly, a confidence level for the standard deviation of the critical Mach number with discretization error is defined as

$$\Pr \left[\left| \frac{\bar{\sigma}_{M_{cr}}(\Delta) - \sigma_{M_{cr}}(\Delta_{res})}{\sigma_{M_{cr}}(\Delta_{res})} \right| \geq 1 - C_{\sigma_{M_{cr}}}^* \right] \leq 1 - C_{\sigma_{M_{cr}}}^* \quad (A5)$$

The corresponding confidence level $C_{\sigma_{M_{cr}}}^*$ is then obtained as

$$C_{\sigma_{M_{cr}}}^* = 2 - (2 - C_{\sigma_{M_{cr}}})(1 + \epsilon_{\sigma_{M_{cr}}}(\Delta)) \quad (A6)$$

In the case of crude Monte Carlo reliability analysis, the confidence level is based on the estimation of the mean of the indicator function in Eq. (58). The influence of the discretization error on the confidence level follows then from Eq. (A4) as

$$C_{p_{fail}}^* = 1 - |\epsilon_{\mu_I}(\Delta)| - (1 - C_{p_{fail}})(1 + \epsilon_{\sigma_I}(\Delta)) \quad (A7)$$

Using $\mu_I = p_{fail}$ and $\sigma_I = \sqrt{p_{fail} - p_{fail}^2}$ this expression can be written as

$$C_{p_{fail}}^* = 1 - |\epsilon_{p_{fail}}(\Delta)| - (1 - C_{p_{fail}}) \sqrt{\frac{p_{fail}(\Delta) - p_{fail}^2(\Delta)}{p_{fail}(\Delta_{res}) - p_{fail}^2(\Delta_{res})}} \quad (A8)$$

Finally, in the case of importance sampling, the confidence level with discretization error influence is obtained as

$$C_{\mu_I}^* = 1 - |\epsilon_{p_{fail}}(\Delta)| - (1 - C_{\mu_I}) \frac{p_{fail}(\Delta)}{p_{fail}(\Delta_{res})} \quad (A9)$$

Acknowledgments

The MicroNed program (part of the BSIK program of the Dutch government) is acknowledged for supporting the research of Clemens Verhoosel.

References

- [1] Bisplinghoff, R. L., *Aeroelasticity*, Addison Wesley Longman, Cambridge, MA, 1955.
- [2] Dowell, E. H., *A Modern Course in Aeroelasticity*, Kluwer Academic, Norwell, MA, 2004.
- [3] Farhat, C., Lesoinne, M., and LeTallec, P., "Load and Motion Transfer Algorithms for Fluid/Structure Interaction Problems with Non-Matching Discrete Interfaces: Momentum and Energy Conservation, Optimal Discretization and Application to Aeroelasticity," *Computer Methods in Applied Mechanics and Engineering*, Vol. 157, No. 1–2, April 1998, pp. 95–114. doi:10.1016/S0045-7825(97)00216-8
- [4] Gutiérrez, M. A., and Krenk, S., *Stochastic Finite Element Methods, Encyclopedia of Computational Mechanics*, Wiley, New York, 2004, pp. 657–681.
- [5] Kornecki, A., Dowell, E. H., and O'Brien, J., "Aeroelastic Instability of 2-Dimensional Panels in Uniform Incompressible-Flow," *Journal of Sound and Vibration*, Vol. 47, No. 2, 1976, pp. 163–178. doi:10.1016/0022-460X(76)90715-X
- [6] Piperno, S., and Farhat, C., "Partitioned Procedures for the Transient Solution of Coupled Aeroelastic Problems - Part II: Energy Transfer Analysis and Three-Dimensional Applications," *Computer Methods in Applied Mechanics and Engineering*, Vol. 190, No. 24–25, 2001, pp. 3147–3170. doi:10.1016/S0045-7825(00)00386-8
- [7] Miles, J. W., *The Potential Theory of Unsteady Supersonic Flow*, Cambridge Univ. Press, Cambridge, England, UK, 1959.
- [8] Kornecki, A., "Static and Dynamic Instability of Panels and Cylindrical-Shell in Subsonic Potential Flow," *Journal of Sound and Vibration*, Vol. 32, No. 2, 1974, pp. 251–263. doi:10.1016/S0022-460X(74)80168-9
- [9] Higham, N., Mackey, D., Tisseur, F., and Garvey, S., "Scaling, Sensitivity and Stability in the Numerical Solution of Quadratic Eigenvalue Problems," *International Journal for Numerical Methods in Engineering*, Vol. 73, No. 3, 2008, pp. 344–360. doi:10.1002/nme.2076
- [10] Vanmarcke, E., *Random Fields: Analysis and Synthesis*, MIT Press, Cambridge, MA, 1983.
- [11] Der Kiureghian, A., and Liu, P. L., "Structural Reliability Under Incomplete Probability Information," *Journal of Engineering Mechanics*, Vol. 112, No. 1, Jan. 1986, pp. 85–104.
- [12] Huang, S. P., Quek, S. T., and Phoon, K. K., "Convergence Study of the Truncated Karhunen–Loève Expansion for Simulation of Stochastic Processes," *International Journal for Numerical Methods in Engineering*, Vol. 52, No. 9, Nov. 2001, pp. 1029–1043. doi:10.1002/nme.255
- [13] Spanos, P. D., and Ghanem, R., "Stochastic Finite Element Expansion for Random Media," *Journal of Engineering Mechanics*, Vol. 115, No. 5, May 1989, pp. 1035–1053.
- [14] Gutiérrez, M. A., Verhoosel, C., and Hulshoff, S., "Fluid–Structure Interaction Analysis of a Plate with a Random Field of Elastic Properties," *Proceedings ICOSAR*, edited by G. Augusti, G. Schueller, and M. Campioli, Millpress, Rotterdam, The Netherlands, 2005, pp. 3167–3173.
- [15] Cochran, W., *Sampling Techniques*, 3rd ed., Wiley, New York, 1977.
- [16] Kenney, J. F., and Keeping, E. S., *Mathematics of Statistics*, Van Nostrand, Princeton, NJ, 1954.
- [17] Adhikari, S., and Friswell, M. I., "Random Matrix Eigenvalue Problems in Structural Dynamics," *International Journal for Numerical Methods in Engineering*, Vol. 69, No. 3, Jan. 2007, pp. 562–591. doi:10.1002/nme.1781
- [18] Liu, P. L., and Der Kiureghian, A., "Optimization Algorithms for Structural Reliability," *Structural Safety*, Vol. 9, No. 3, Feb. 1991, pp. 161–177. doi:10.1016/0167-4730(91)90041-7

- [19] Breitung, K., "Asymptotic Approximations for Multinormal Integrals," *Journal of Engineering Mechanics*, Vol. 110, No. 3, 1984, pp. 357–366. doi:10.2514/3.7211
- [20] Plaut, R. H., and Huseyin, K., "Derivatives of Eigenvalues and Eigenvectors in Non-Self-Adjoint Systems," *AIAA Journal*, Vol. 11, No. 2, 1973, pp. 250–251. doi:10.2514/3.6740
- [21] Nelson, R. B., "Simplified Calculation of Eigenvector Derivatives," *AIAA Journal*, Vol. 14, No. 9, 1976, pp. 1201–1205.
- [22] Guedria, N., Chouchane, M., and Smaoui, H., "Second-Order Eigensensitivity Analysis of Asymmetric Damped Systems Using Nelson's Method," *Journal of Sound and Vibration*, Vol. 300, No. 3–5, March 2007, pp. 974–992. doi:10.1016/j.jsv.2006.09.003

N. Alexandrov
Associate Editor